ISSN 1063-7834, Physics of the Solid State, 2018, Vol. 60, No. 7, pp. 1425–1431. © Pleiades Publishing, Ltd., 2018.
Original Russian Text © M.N. Volochaev, S.V. Komogortsev, V.G. Myagkov, L.E. Bykova, V.S. Zhigalov, N.P. Shestakov, D.A. Velikanov, D.A. Smolyakov, A.V. Luk'yanenko, V.B. Rachek, Yu.Yu. Loginov, I.A. Tambasov, A.A. Matsynin, 2018, published in Fizika Tverdogo Tela, 2018, Vol. 60, No. 7, pp. 1409–1415.

SURFACE PHYSICS AND THIN FILMS

Structural and Magnetic Characteristics of Nanogranular Co–Al_2O_3 Single- and Multilayer Films Formed by the Solid-State Synthesis

M. N. Volochaev[a, b, *], S. V. Komogortsev[a], V. G. Myagkov[a], L. E. Bykova[a], V. S. Zhigalov[a], N. P. Shestakov[a], D. A. Velikanov[a], D. A. Smolyakov[a], A. V. Luk'yanenko[a, c], V. B. Rachek[c], Yu. Yu. Loginov[b], I. A. Tambasov[a], and A. A. Matsynin[a]

[a] *Kirensky Institute of Physics, Krasnoyarsk Scientific Center, Siberian Branch, Russian Academy of Sciences, Krasnoyarsk, 660036 Russia*

[b] *Siberian State University of Science and Technology, Krasnoyarsk, 660014 Russia*

[c] *Siberian Federal University, Krasnoyarsk, 660041 Russia*

**e-mail: volochaev91@mail.ru*

Received January 24, 2018

Abstract—The results of structural and magnetic investigations of nanogranular Co–Al_2O_3 films formed from Co_3O_4/Al thin-film layered structures upon vacuum annealing are reported. The Co_3O_4/Al films have been obtained by sequential reactive magnetron sputtering of a metallic cobalt target in a medium consisting of the Ar + O_2 gas mixture and magnetron sputtering of an aluminum target in the pure argon atmosphere. It is shown that such a technique makes it possible to obtain nanogranular Co–Al_2O_3 single- and multilayer thin films with a well-controlled size of magnetic grains and their distribution over the film thickness.

DOI: 10.1134/S1063783418070302

1. INTRODUCTION

Nanogranular thin films containing ferromagnetic (Co, Fe, Ni) nanoparticles distributed in a semiconductor or dielectric matrix based on metal oxides (In_2O_3, TiO_2, SnO_2, Al_2O_3, ZrO_2, etc.) characterized by the unique combination of magnetic and electrical properties are promising for application in spintronic devices, high-density magnetic memory [1, 2], thermoelectric converters [3], magnetic field sensors [4], catalysis [5], and medicine [6]. Of particular importance is the search for inexpensive high-efficiency techniques for forming such structures. To date, both physical [7–9] and chemical [5, 10, 11] methods for obtaining thin-film nanocomposites are available and widely used.

In our previous work [12], we proposed a simple high-efficiency technique of solid-state synthesis of nanogranular magnetic films, which is based on thermite reactions between thin ferromagnetic metal oxide layers and a reducing metal. In this technique, the reagents are selected so that the enthalpy of their formation was higher than the enthalpy of formation of reaction products. The synthesized films consist of ferromagnetic (Fe, Co) nanograins uniformly distributed over an oxide (In_2O_3, ZrO_2, or Al_2O_3) matrix and exhibit simultaneously the magnetic and semiconductor (dielectric) properties combined with the high chemical, thermal, and time stability [12–15]. The key parameters that determine the properties of the synthesized films of the same chemical composition are the size and shape of magnetic grains and density of their distribution in a matrix [16]. The technique described in [12–15] was limited by the fact that a ferromagnetic metal oxide (Fe_2O_3 or Co_3O_4) was obtained by thermal oxidation of a metallic (Fe or Co) film in air. This technique can be only used to obtain bilayer thin-film reagents. The method for forming ferromagnetic metal oxide films proposed in this study is based on reactive magnetron sputtering of a ferromagnetic metal target in the of Ar + O_2 gas mixture atmosphere. This method, which allows repositioning of reagents and fabricating multilayer structures, has been successfully tested in the synthesis of nanogranular Co–Al_2O_3 films from Co_3O_4/Al layered thin-film reagents in the course of the termite reaction $3Co_3O_4 + 8Al = 4Al_2O_3 + 9Co$ [15]. Here, we present the results of structural investigations of the Co–Al_2O_3 films (morphology, phase composition, and dependences of the size, shape, and distribution density of magnetic cobalt grains on the initial Co_3O_4 layer thickness) synthesized from the Co_3O_4/Al bilayers and a substrate/$(Co_3O_4/Al)_{10}$ multilayer structure.

2. EXPERIMENTAL

Thin-film Co_3O_4 cobalt oxide layers were obtained by high-frequency reactive sputtering of a metallic

cobalt (99.99% pure) target in the Ar (70%) + O_2 (30%) gas mixture atmosphere at a residual pressure of 2.6×10^{-3} Torr in a chamber. The Al layers were formed by low-frequency magnetron sputtering of an aluminum (99.99% pure) target in the pure argon (99.999%) atmosphere.

To study the structural characteristics (morphology, phase composition, size and shape of magnetic cobalt grains, and their distribution density) as functions of the initial Co_3O_4 layer thickness, we fabricated a series of Co_3O_4/Al films with cobalt oxide layer thicknesses of 10, 15, 20, 40, 60, 80, and 100 nm on single-crystal NaCl (001) substrates; the layer thickness ratio was Co_3O_4 : Al = 1 : 0.8. After deposition, the films were annealed in vacuum at a residual pressure of 10^{-6} Torr and an annealing temperature of 550°C (at the higher annealing temperatures, NaCl starts intensely evaporating and settling on the chamber walls) for 1 h. The films were then separated from the substrates in distilled water and deposited on supporting grids for transmission electron microscopy study and annealed once again in vacuum at a residual pressure of 10^{-6} Torr and a temperature of 700°C to complete the synthesis [15].

To study the effect of the layer sequence in the initial thin-film bilayers on the structural and magnetic characteristics of the Co–Al_2O_3 films, Co_3O_4/Al and Al/Co_3O_4 films with respective cobalt and aluminum layer thicknesses of 20 and 30 nm were deposited onto the NaCl (001) and glass ceramic substrates. Increasing the aluminum oxide layer thickness, one can obtain the maximum possible reduction rate and investigate the films for secondary reaction products (cobalt–aluminum compounds or ternary cobalt, aluminum, and oxygen compounds) formed. After deposition, the films were also annealed in vacuum at a residual pressure of 10^{-6} Torr and an annealing temperature of 700°C for 1 h.

To synthesize nanogranular Co–Al_2O_3 multilayers, 15-nm-thick Co_3O_4 layers and 12-nm-thick Al layers were sequentially deposited onto a silicon substrate to obtain a Si/$(Co_3O_4/Al)_{10}$ thin-film structure, which was annealed in vacuum at a temperature of 700°C and a residual pressure of 10^{-6} Torr for 1 h.

Structural study of the synthesized films was carried out using transmission electron microscopy (TEM) on a Hitachi HT7700 microscope at an accelerating voltage of 100 kV. Cross sections were prepared using a Hitachi FB2100 (FIB) single-beam focused ion beam system in accordance with the procedure described in [17, 18], in which samples are coated with a amorphous germanium film to ensure the fracture protection during cutting. The surface relief was examined on a Nanolnk DPN5000 atomic force microscope. Saturation magnetization M_S and coercivity H_C, as well as the shape of hysteresis loops in the film plane and perpendicular to it, were measured on a vibrating-sample magnetometer in magnetic fields of up to 10 kOe at room temperature.

Table 1. Interpretation of the diffraction pattern (Fig. 1b)

Ring no.	γ-Al_2O_3	β-Co	CoO
1	(111)		
2	(220)		
3	(311)		
4			(200)
5		(111)	
6	(400)		
7		(200)	
8	(511)		
9			(220)
10	(440)		
11		(220)	
12	(444)		
13		(311)	

3. RESULTS AND DISCUSSION

3.1. Nanogranular Co–Al_2O_3 Single-Layer Films

Figure 1a shows a TEM image of the synthesized Co–Al_2O_3 film with an initial Co_3O_4 layer thickness of 15 nm. The film contains cobalt nanograins, mostly spherical, which are uniformly distributed in the aluminum oxide matrix. The inset in Fig. 1a shows a histogram of the distribution of percentage of cobalt particles as a function of their size. It can be seen that the distribution is normal and the average particle size is 25 nm. Figure 1b shows the electron diffraction pattern obtained from an area 10 μm in diameter. The interpretation of the diffraction pattern (Table 1) revealed the presence of the high-temperature γ-Al_2O_3 alumina phase, metal β-Co, and weak reflections of the CoO cobalt oxide phase. Figure 1c shows a high-resolution TEM image of the Co–Al_2O_3 film, in which one can clearly see that the particles have a 2–3-nm-thick shell. Since the shell contrast is darker than the contrast of the nanocrystalline Al_2O_3 matrix, the average atomic weight of the shell is greater than that of Al_2O_3, which is indicative of the presence of cobalt in its composition.

Since the diffraction pattern contains weak CoO phase reflections, we may conclude that the particle shell consists of nanocrystalline CoO. The similar results were obtained for the rest films; the films only differed in grain size and shape; the shell thickness was no larger than 4 nm.

Figure 2 shows the dependence of the average Co particle size on the initial Co_3O_4 layer thickness. The sampling for the histogram (inset in Fig. 1a) and plot (Fig. 2) consisted of no less than one and a half thou-

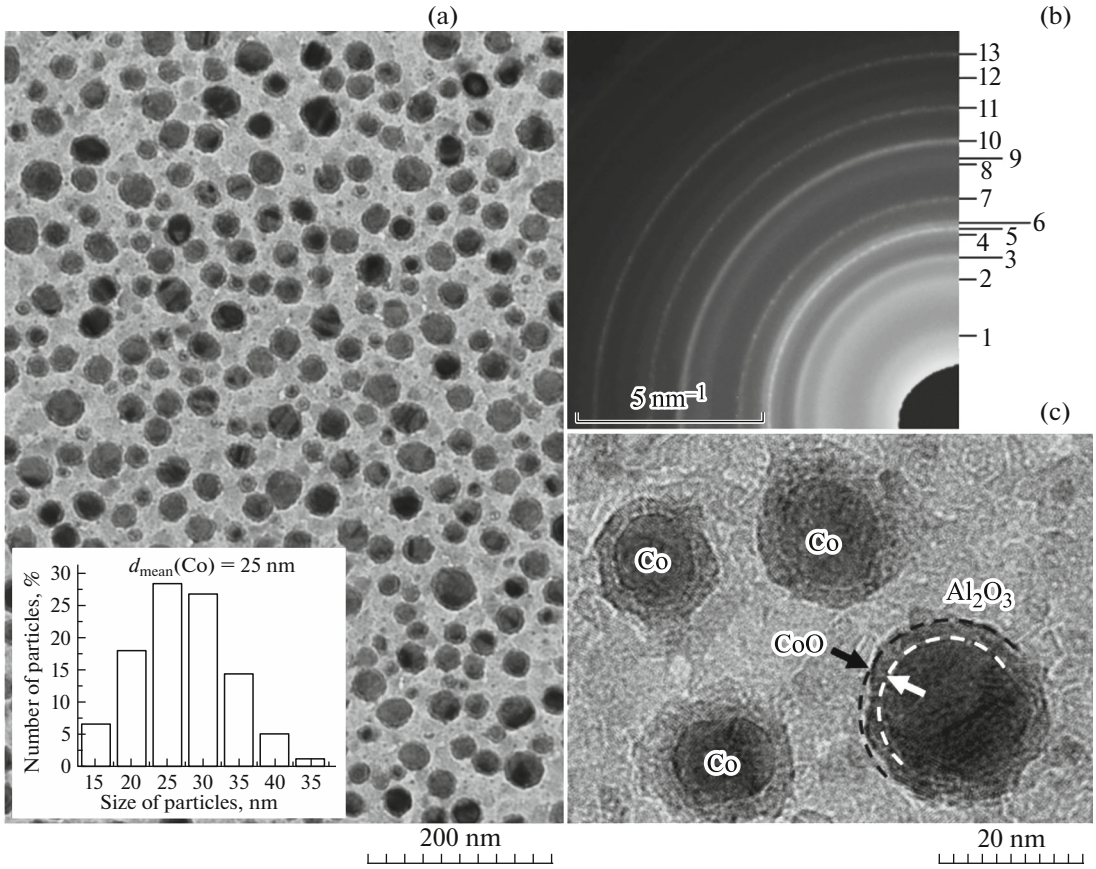

Fig. 1. (a) TEM image, (b) microdiffraction pattern, and (c) high-resolution TEM image of the Co–Al_2O_3 film.

sand particles for each sample. Particles with a content of lower than 0.5% were not included in the calculations. Dots show the experimental data and dash-and-dot line, the approximation. The results obtained show that the dependence is almost linear. It should be noted that as the initial Co_3O_4 layer thickness increases, the particles are stronger extended and their dispersion increases; however, the particle sizes remain within the same order of magnitude.

Note that the size and shape of nanograins formed are also affected by other factors, including heat conductivity and structure of the substrate and annealing temperature and time. For example, the experiments on annealing the films separated from the substrates immediately after deposition revealed a sharp increase in the average size and dispersion of cobalt nanograins and, at an initial cobalt oxide layer thickness of 80 nm and more, a continuous cobalt film forms.

In our previous work [15], the synthesized Co–Al_2O_3 films contained the α-Al_2O_3, α-Co, β-Co, and $CoAl_2O_4$ phases; the particle sizes differed by an order of magnitude and the initial cobalt layer thickness was 20 nm (or 30 nm for Co_3O_4). The results reported here show the better film quality, which is indicative of the obvious advantages of forming the ferromagnetic metal oxide by magnetron sputtering over thermal oxidation of a metallic cobalt film in the air medium [14, 15].

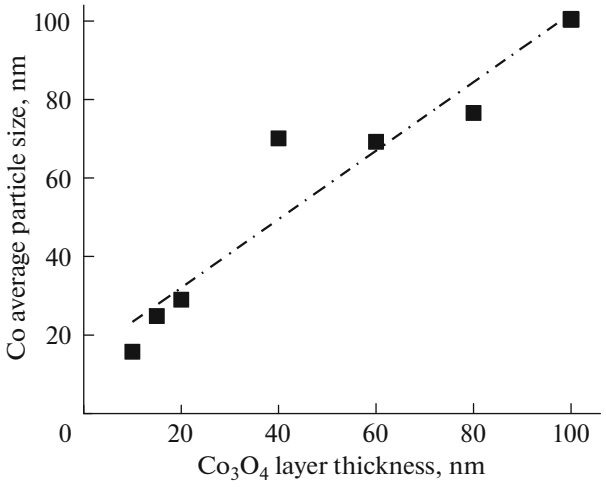

Fig. 2. Dependence of the average cobalt nanograin size on the initial Co_3O_4 layer thickness.

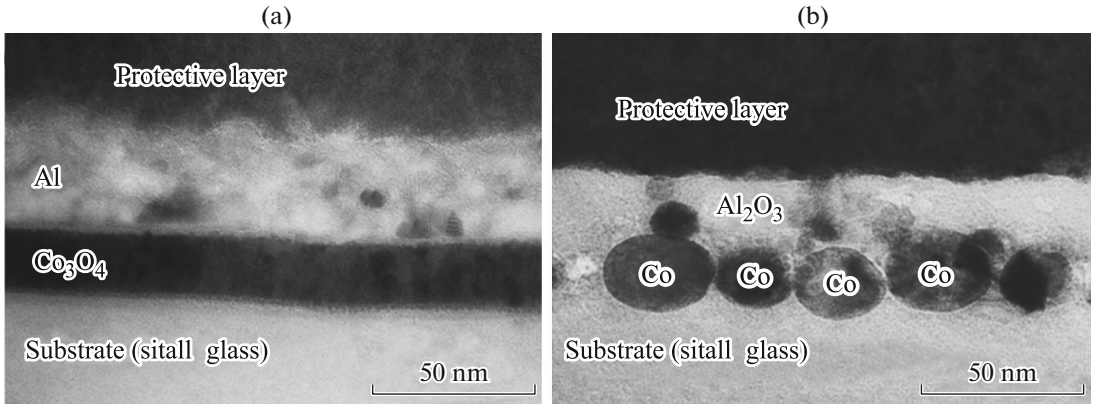

Fig. 3. TEM images of (a) the initial Co_3O_4/Al film cross section and (b) synthesized Co–Al_2O_3 film.

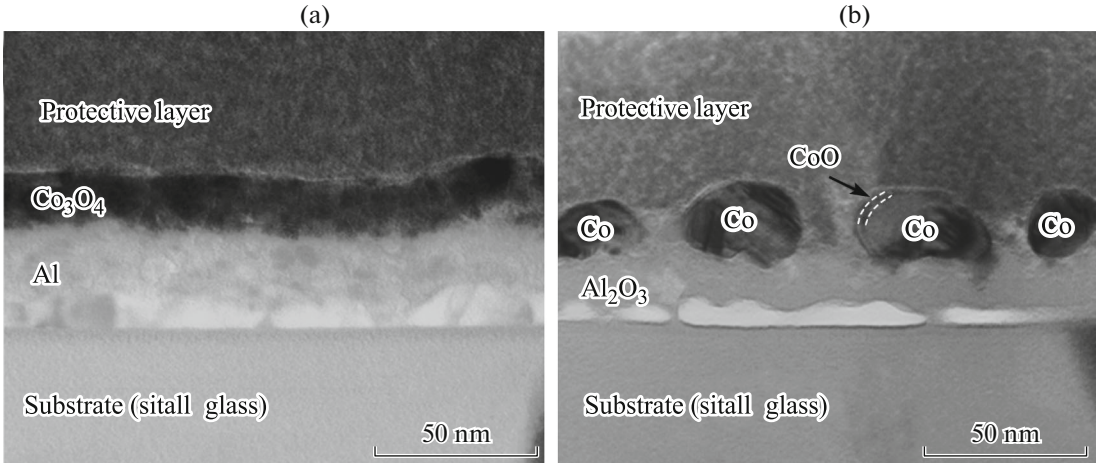

Fig. 4. TEM images of the Al/Co_3O_4 film cross section (a) in the initial state and (b) after the thermite reaction.

Figure 3a shows a TEM image of the initial Co_3O_4/Al film cross section. One can clearly see the aluminum and cobalt oxide layers with the pronounced interface without traces of intermixing. The cross-sectional image of the same film after annealing at a temperature of 700°C is presented in Fig. 3b. The formation of ellipsoidal cobalt nanograins partly immersed in the substrate and surrounded by the Al_2O_3 matrix is observed.

The results of TEM study of the Al/Co_3O_4 films in the cross-sectional geometry before and after annealing are shown in Figs. 4a and 4b, respectively. In this case, cobalt nanograins form on the alumina layer surface.

The average nanograin size is the same in both cases; however, it is somewhat (by about 40 nm) larger than in the films on the NaCl substrate (Fig. 2); no phase composition differences are observed. In addition, the brighter shell with a thickness of about 2 nm is observed around the particles, although it is not as pronounced as in the films on the NaCl substrate. The lack of clear shell contrast can be related to the formation of a destructed layer during preparation of cross sections, which can have a thickness of up to ~20 nm [19].

Figure 5 shows an AFM image of the surface of a Co–Al_2O_3 film synthesized from the Al/Co_3O_4 film bilayer, where one can clearly see the particles uniformly distributed over the sample surface. The particle surface fraction is $\sigma \approx 0.31 \pm 0.05$. The nanograin synthesis on the surface makes it possible to broaden the range of potential application of nanograin films as catalytically active coatings in hydrogenation and reduction reactions [20] or as catalytically active centers in growing nanotube arrays [21]. Since the particles are tightly bound to the oxide base, such coatings will have the high thermal stability and wear resistance.

The saturation magnetization measurements (Fig. 6) allow us to estimate the degree of pure cobalt recovery. The magnetization value calculated by reducing the magnetic moment to the total cobalt vol-

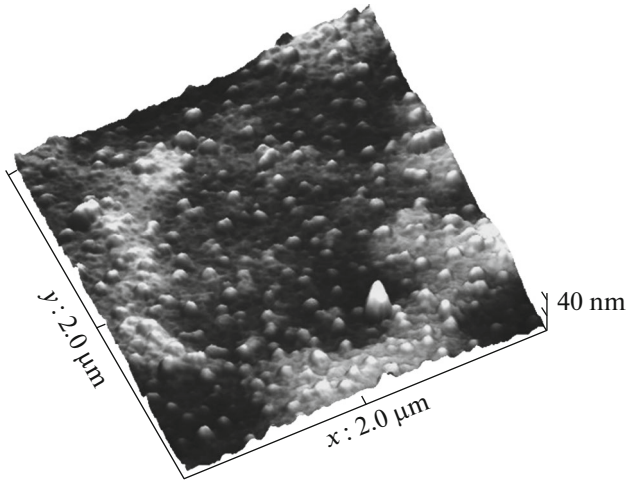

Fig. 5. AFM image of the synthesized Co–Al_2O_3 film.

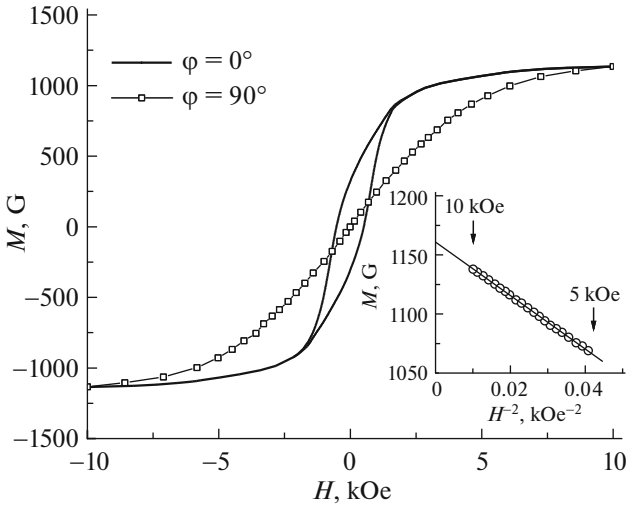

Fig. 6. Magnetization curves of the nanogranular Co–Al_2O_3 films in the film plane (φ = 0°) and perpendicular to it (φ = 90°).

ume in a sample (assuming Co to be represented by only a fcc phase) approaches the saturation in accordance with the Akulov law $M = M_S(1 - (\alpha \times 2K/M_SH)^2)$ (see the inset in Fig. 6), where K is the grain anisotropy constant, M_S is the saturation magnetization, and α is the coefficient taking the values $(1/15)^{1/2}$ for the uniaxial anisotropy and $(2/105)^{1/2}$ for the triaxial anisotropy [22, 23]. In this case, the saturation magnetization was found to be $M_S = (1160 \pm 20)$ G. The value understated in comparison with the saturation magnetization of pure fcc Co ($M_{S\_fcc} = 1400$ G) can be attributed to the incomplete cobalt reduction, so $M_S = M_{S\_fcc}\eta$, where η is the degree of reduction. Thus, the degree of reduction can be estimated as $\eta = M_S/M_{S\_fcc} = 0.83 \pm 0.02$. The remaining cobalt is most likely localized in the grain shells, where the CoO phase traces are observed.

The obtained η value agrees well with the estimate based on the analysis of TEM images. In the case of spherical grains, the volume fraction of the shell is $\delta V = (V_0 - V)/V_0 = (R_0^3 - R_3)/R_0^3$, where V and R are the volume and radius of a grain without shell and V_0 and R_0 are the volume and radius of a particle with the shell. Based on the TEM data (Fig. 4b), we take the radius of a grain without shell to be 20 nm and the shell thickness, to be 2 nm, i.e., $R_0 = 22$ nm; thus, we obtain $\delta V \approx 0.25$. Using the ratio between the CoO (6.45 g/cm^3) and metallic fcc cobalt (8.9 g/cm^3) densities, we can calculate the cobalt fraction in the $\delta V_{Co} \approx 0.18$. Consequently, the fraction of cobalt contained in the grain cores is $\eta' = 1 - \delta V_{Co} = 0.82$, which agrees with the estimated degree of reduction $\eta = 0.83 \pm 0.02$. The coefficient α in the Akulov law can be chosen $(1/15)^{1/2}$. Even in this case, the estimated grain anisotropy constant $K \approx 2.9 \times 10^6$ erg/cm^3 is significantly higher than the magnetocrystalline anisotropy constant of fcc Co ($K_{fcc\_Co} \approx 1 \times 10^6$ erg/cm^3) [24–27].

This situation is typical of nanoparticles with the magnetic anisotropy determined by the surface effects directly related to the matrix type and the particle shape [28–32]. The particle blocking temperature estimated as $T_B = KV/(25k_B) \approx 1400$ K (K is the grain anisotropy constant, V is the grain volume, and k_B is the Boltzmann constant) even in the smallest grains ($D = 15$ nm) is much higher than room temperature; thus, the magnetic properties reported here can be considered regardless of the heat relaxation processes.

The films are characterized by the easy-plane magnetic anisotropy (Fig. 6) caused by the dipole-dipole magnetic coupling between grains. The magnetic anisotropy constant estimated from the experimental magnetization curves as the difference between the works on magnetizing along the two different directions is $K_\perp = \int (M(H)_\perp - M(H)_\parallel) dH$ is $K_\perp = -(2.04 \pm 0.05) \times 10^6$ erg/cm^3. Taking into account that the magnetic anisotropy in granular films related to the dipole-dipole interaction is determined by the volume fraction of grains (ν) and magnetization $K_\perp = -2\pi M_S^2 \nu$ [33–35], we can make the estimation $\nu = 0.24 \pm 0.05$. The obtained value is in good agreement with the TEM (Fig. 4b) and AFM microscopy data (Fig. 5).

3.2. Nanogranular Co–Al_2O_3 Multilayer Films

Figure 7a presents an electron microscopy image of the cross section of the Co–Al_2O_3 nanogranular multilayer film obtained from the Si/$(Co_3O_4/Al)_{10}$ layered structure by the solid-phase synthesis. The synthesized film consists of ten cobalt nanograin layers separated by the alumina spacers; the film thickness is ~240 nm. In Fig. 7b, one can see an enlarged film fragment showing that the average particle size is about

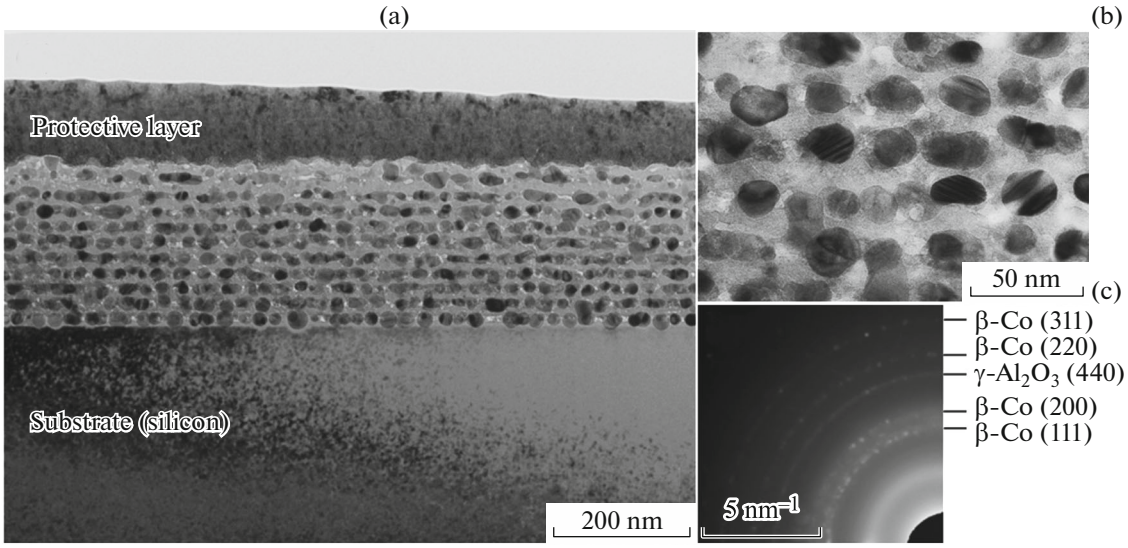

Fig. 7. (a) TEM image of the nanogranular Co–Al_2O_3 multilayer film cross section. (b) Enlarged fragment of this image. (c) Microdiffraction pattern corresponding to (a).

20–25 nm and the average interparticle spacing is 5–10 nm. As the distance from the substrate increases, the particles lose their spherical shape and their size increases, especially in the last two layers, which is most likely due to the reduction of heat dissipation from the substrate in these layers as compared with the layers located closer to the substrate.

The electron diffraction pattern in Fig. 7c contains sharp reflections of the cobalt fcc phase and (440) reflection from of the γ-Al_2O_3 matrix. The diffuse halos in the diffraction pattern are caused by the silicon substrate amorphization during processing the sample preparation by an ion beam [19].

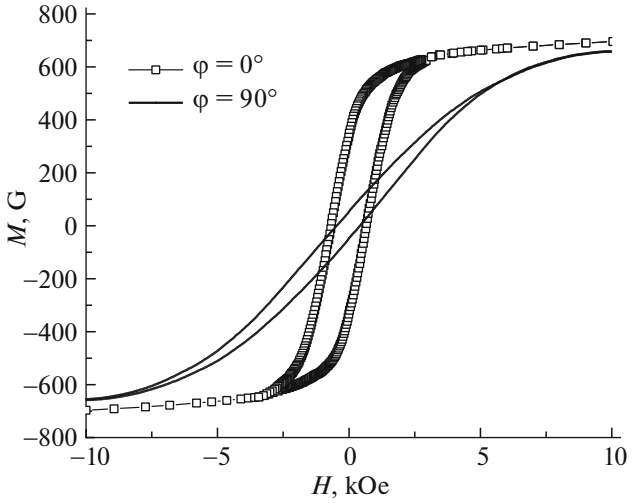

Fig. 8. Magnetization curves of the nanogranular Co–Al_2O_3 multilayered films in the film plane (φ = 0°) and perpendicular to it (φ = 90°).

The magnetization of a multilayer granular sample, as well as of a single-layer film, reduced to the total cobalt volume is lower than in the single-layer sample (Fig. 8). Here, the degree of reduction is $\eta = M_S/M_{S\_fcc} = 0.50 \pm 0.05$. The lower-efficiency reduction as compared with the results obtained for the single-layer Co–Al_2O_3 films is apparently due to the insufficient amount of aluminum in this multilayer sample.

In addition, the granular multilayer films are characterized by the easy-plane magnetic anisotropy, but, in this case, it is more pronounced. This magnetic anisotropy constant estimated from the magnetization curves, as in the single-layer film, is $K_\perp = -(1.58 \pm 0.04) \times 10^6$ erg/cm^3. This is lower than in the single-layer film, since the magnetization of this sample is lower. However, the volume fraction of grains estimated as was made above for the single-layer film is $\nu = 0.58 \pm 0.05$. This explains the large remanent magnetization during magnetizing in the film plane, since at the high degree of filling with grains it should lead to the greater rectangularity of the hysteresis loop.

4. CONCLUSIONS

Nanogranular Co–Al_2O_3 films were synthesized in the course of a thermite reaction in Co_3O_4/Al thin-film structures obtained by sequential reactive magnetron sputtering of a metallic cobalt target in the Ar + O_2 gas mixture atmosphere and magnetron sputtering of an aluminum target in pure argon.

The synthesized films contain β-Co nanograins in the CoO shell uniformly distributed in the γ-Al_2O_3 matrix. It was established that the average size of the synthesized cobalt nanograins depends linearly on the

initial reagent thickness in the thickness range of 10–100 nm. The synthesis of the Co_3O_4 layer by high-frequency reactive sputtering makes it possible to obtain the $Co–Al_2O_3$ thin films with cobalt nanograins located on the film surface.

Nanograin $Co–Al_2O_3$ multilayer films consisting of ten layers of cobalt nanograins surrounded by Al_2O_3 spacers were fabricated by the solid-state reaction from the $(Co_3O_4/Al)_{10}$ thin-film multilayer.

The magnetization of the granular single- and multilayered sample yields degrees of cobalt reduction in the thermite reaction of 0.83 ± 0.02 and 0.50 ± 0.05, respectively. The measurement of magnetic anisotropy of the granular films allowed us to estimate the volume fraction of grains as 0.24 ± 0.05 for the single-layer and 0.58 ± 0.05 for multilayer films.

ACKNOWLEDGMENTS

This study was supported by the Russian Foundation for Basic Research, project no. 16-03-00069 and the Russian Foundation for Basic Research, Government of the Krasnoyarsk Territory, and Krasnoyarsk Territorial Foundation for Support of Scientific and R&D Activities, project no. 18-42-243010 r_mol_a.

REFERENCES

1. S.-C. Chen, P. C. Kuo, A. C. Sun, C. T. Lie, and W. C. Hsu, Mater. Sci. Eng. B **88**, 91 (2002).
2. L. Zhang, W. W. Zhong, S. S. Yu, S. X. Xue, Y. P. Liu, Z. G. Li, and W. P. Chen, J. Alloys Compd. **560**, 177 (2013).
3. A. V. Dmitriev and I. P. Zvyagin, Phys. Usp. **53**, 789 (2010).
4. J. Garcia-Torres, E. Valles, and E. Gomez, J. Magn. Magn. Mater. **322**, 3186 (2010).
5. X. Zhang, R. Hu, Y. Liu, J. Zhao, L. Hou, D. Yang, Z. Hao, and H. Su, Int. J. Hydrogen Energy **40**, 10026 (2015).
6. S. M. H. AL-Jawad, A. A. Taha, and M. M. Salim, Optik **142**, 42 (2017).
7. J. C. Denardin, M. Knobela, X. X. Zhang, and A. B. Pakhomov, J. Magn. Magn. Mater. **262**, 15 (2003).
8. T. N. Koltunowicz, P. Zukowski, J. Sidorenko, V. Bayev, J. A. Fedotova, M. Opielak, and A. Marczuk, J. Magn. Magn. Mater. **421**, 98 (2017).
9. Y. Gao, J. Lu, and G. Han, Phys. B (Amsterdam, Neth.) **458**, 40 (2015).
10. L. Benea, P. Ponthiaux, and F. Wenger, Surf. Coat. Technol. **205**, 5379 (2011).
11. S. A. Singh, B. Vemparala, and G. Madras, J. Environ. Chem. Eng. **3**, 2684 (2015).
12. V. G. Myagkov, I. A. Tambasov, O. A. Bayukov, V. S. Zhigalov, L. E. Bykova, Y. L. Mikhlin, M. N. Volochaev, and G. N. Bondarenko, J. Alloys Compd. **612**, 189 (2014).
13. V. G. Myagkov, L. E. Bykova, O. A. Bayukov, V. S. Zhigalov, I. A. Tambasov, S. M. Zharkov, A. A. Matsynin, and G. N. Bondarenko, J. Alloys Compd. **636**, 223 (2015).
14. V. G. Myagkov, V. S. Zhigalov, L. E. Bykova, S. M. Zharkov, A. A. Matsynin, M. N. Volochaev, I. A. Tambasov, and G. N. Bondarenko, J. Alloys Compd. **665**, 197 (2016).
15. V. G. Myagkov, L. E. Bykova, V. S. Zhigalov, A. A. Matsynin, M. N. Volochaev, I. A. Tambasov, Yu. L. Mikhlin, and G. N. Bondarenko, J. Alloys Compd. **724**, 820 (2017).
16. A. Granovsky, Yu. Kalinin, A. Sitnikov, and O. Stognei, Phys. Proc. **82**, 46 (2016).
17. M. N. Volochaev, Yu. Yu. Loginov, and M. V. Savel'eva, Molodezh'. Ob-vo. Sovrem. Nauka, Tekh. Innov. **14**, 287 (2015).
18. M. N. Volochaev and Yu. Yu. Loginov, Vestn. SibGAU **17**, 792 (2016).
19. J. Mayer, L. A. Giannuzzi, T. Kamino, and J. Michael, MRS Bull. **32**, 400 (2007).
20. Yu. V. Popov, V. M. Mokhov, D. N. Nebykov, and I. I. Budko, Izv. VolgGTU **12**, 5 (2014).
21. H. Sugime, S. Esconjauregui, J. Yang, L. D'Arsie, R. A. Oliver, S. Bhardwaj, C. Cepek, and J. Robertson, Appl. Phys. Lett. **103**, 073116 (2013).
22. N. Akulov, Z. Phys. **81**, 790 (1933).
23. R. S. Iskhakov and S. V. Komogortsev, Phys. Met. Metallogr. **112**, 666 (2011).
24. D. S. Rodbell, J. Appl. Phys. **29**, 311 (1958).
25. J. C. Anderson, Proc. Phys. Soc. **75**, 33 (1960).
26. C. W. Berghout, J. Phys. Chem. Solids **24**, 507 (1963).
27. D. G. Lord and J. Goddard, Phys. Status Solidi **37**, 665 (1970).
28. H. K. Lachowicz, A. Sienkiewicz, P. Gierlowski, and A. Ślawska-Waniewska, J. Appl. Phys. **88**, 368 (2000).
29. M. Hillenkamp, S. Oyarzún, N. Troc, J. Ramade, A. Tamion, F. Tournus, V. Dupuis, and V. Rodrigues, Eur. Phys. J. D **71**, 330 (2017).
30. S. V. Komogortsev, R. S. Iskhakov, Ch. N. Barnakov, N. A. Momot, V. K. Mal'tsev, and A. P. Kozlov, Fiz. Met. Metallogr. **109**, 1 (2010).
31. A. A. Dubrovskiy, D. A. Balaev, K. A. Shaykhutdinov, O. A. Bayukov, O. N. Pletnev, S. S. Yakushkin, G. A. Bukhtiyarova, and O. N. Martyanov, J. Appl. Phys. **118**, 213901 (2015).
32. D. A. Balaev, I. S. Poperechny, A. A. Krasikov, K. A. Shaikhutdinov, A. A. Dubrovskiy, S. I. Popkov, A. D. Balaev, S. S. Yakushkin, G. A. Bukhtiyarova, O. N. Martyanov, and Y. L. Raikher, J. Appl. Phys. **117**, 63908 (2015).
33. V. A. Ignatchenko, I. S. Edelman, and D. A. Petrov, Phys. Rev. B **81**, 54419 (2010).
34. E. A. Denisova, S. V. Komogortsev, R. S. Iskhakov, L. A. Chekanova, A. D. Balaev, Y. E. Kalinin, and A. V. Sitnikov, J. Magn. Magn. Mater. **440**, 221 (2017).
35. S. V. Komogortsev, E. A. Denisova, R. S. Iskhakov, A. D. Balaev, L. A. Chekanova, Y. E. Kalinin, and A. V. Sitnikov, J. Appl. Phys. **113**, 17C105 (2013).

Translated by E. Bondareva